Applied Catalysis B: Environmental 324 (2023) 122268

Contents lists available at ScienceDirect

Applied Catalysis B: Environmental

journal homepage: www.elsevier.com/locate/apcatb

Roles of structural defects in polycrystalline platinum nanowires for enhanced oxygen reduction activity

Xiao Zhao [a,b,*], Shinobu Takao [b], Yusuke Yoshida [b], Takuma Kaneko [b], Takao Gunji [b], Kotaro Higashi [b], Tomoya Uruga [b,c], Yasuhiro Iwasawa [b,d,*]

[a] Key Laboratory of Automobile Materials of MOE, School of Materials Science and Engineering, Jilin University, Changchun 130012, China
[b] Innovation Research Center for Fuel Cells, The University of Electro-Communications, Chofugaoka, Chofu, Tokyo 182–8585, Japan
[c] Japan Synchrotron Radiation Research Institute, SPring-8, Sayo, Hyogo 679–5198, Japan
[d] Graduate School of Informatics and Engineering, The University of Electro-Communications, Chofugaoka, Chofu, Tokyo 182–8585, Japan

ARTICLE INFO

Keywords:
Oxygen reduction reaction
Polycrystalline nanowires
Atomic steps
Grain boundaries
Catalytic defects

ABSTRACT

Nanocatalysts have uneven reactivity and lively change in reactions, challenging revealing catalytic origins. Phenomenologically, Pt-based nanowires, one of the most important nanostructures, have displayed high activity for oxygen reduction reaction (ORR); however, the fundamentally catalytic origin behind such high performance remains elusive and was implicitly ascribed to one-dimensional structure and/or low-index facets. Here, with molecular-level and operando spectroscopic evidence, we reveal that the polycrystalline platinum nanowires with enhanced ORR activity are closely correlated with structural defects including grain boundaries (GBs), atomic steps, and a few amorphous regions, which is previously neglected or simplified. The local micro-strain is induced by GBs and increases with misorientation angles of GBs. Despite the same coordination number between edge sites and atomic steps, the latter together with a few amorphous regions disturb interfacial water networks via preferably hydrogen bonding, which destabilizes ORR intermediates on terraces and presumably promotes proton transfer.

1. Introduction

Electrocatalysts are crucial in future energy conversion and storage techniques. In response, rational design of efficient electrocatalysts is indispensable and heavily relies on the knowledge on molecular-level electroactive factors and their operating mechanisms [1–10]. However, practical nanoelectrocatalysts are structurally heterogeneous at multi-scales, comprise diverse defects and evolve dynamically in reactions, raising forbidden challenges for an in-depth understanding of electrocatalysts. The Pt-based nanocatalysts remain most-efficient for the oxygen reduction reaction (ORR) [11–18], a crucial reaction for fuel cells and metal-air batteries [11–32]. Typically, polycrystalline Pt-based nanowires (PPNWs), one of the most important nanostructures, have been noted to display enhanced ORR activity; however, it is unclear for underlying reasons for activity enhancement. Two general clues, low-index nanofacets [19,26,33] and one-dimensional (1D) nanostructure, [21,23] have been proposed. However, some puzzles remain for a long time. At first, PPNWs display an unusual size effect. A much higher ORR activity on 1 nm Pt NWs was reported than on 4.5 nm Pt NWs [19] and 200 nm Pt nanotubes, [21,22] distinct from those nanoparticulate catalysts. [34,35].

More importantly, the roles of defects, like atomic steps and grain boundaries (GBs), are elusive in PPNWs. Reports showed both defect-free PPNWs with Pt (111) facet [21–23] and jagged PPNWs with strained and stepped nanofacets [36] had particularly high ORR performance. Steps binding strongly to ORR intermediates were theoretically speculated inactive or low-active for ORR. [35,37,38] However, the acidic ORR activity on high-index facets was reported experimentally higher than on Pt(111). [1] The GBs, thin interfacial regions between grains, are inherent in polycrystals and proposed to induce catalytically active strained domains. [39,40] Practical issues remain unanswered regarding how to tune GBs and thus optimize catalytic performance. More importantly, defects are usually reactive and easily reconstructed in reactions, thereby calling for a site-specific and operando understanding of their electrocatalytic behaviors. For example, evidence emerged that surface charging, for example, producing

* Corresponding authors at: Key Laboratory of Automobile Materials of MOE, School of Materials Science and Engineering, Jilin University, Changchun 130012, China.
E-mail addresses: xzhao417@jlu.edu.cn (X. Zhao), iwasawa@pc.uec.ac.jp (Y. Iwasawa).

https://doi.org/10.1016/j.apcatb.2022.122268
Received 4 September 2022; Received in revised form 8 November 2022; Accepted 4 December 2022
Available online 13 December 2022

oxygenates on defective or oxophilic sites, brings about the disturbance to interfacial water networks and/or double layer [41–43] and subsequently affect intermediates adsorption [41] and/or mass transport. [42] Recent reports reveal defective or disordered $PtNi_x$ catalysts showed better ORR activity than the common $PtNi_x$ alloy at similar crystalline sizes. [39,44–47] Despite those important advances, it remains unexplored in details for whether defects in PPNWs play positive roles, and how they operate in ORR.

Here, we explored molecular-level electroactive factors resulting in enhanced ORR activity for model PPNWs. Experimental evidence reveals PPNWs's defects comprising atomic steps and GBs benefit ORR. Atomic steps on stepped nanofacets disturb interfacial water networks, destabilizing oxygenates adsorption on terraces. The microstrain is induced by GBs and affected by misorientation angles (MOAs) of GBs, inducing higher ORR activity on more disordered/defective PPNWs. Our insights into molecular-level electroactive factors and their operation mechanisms not only rationalize the enhanced ORR activity on PPNWs but also help design of more efficiency nanoelectrocatalysts, for example, by regulating density, architectures, and interfacial chemistry of GBs.

2. Experimental

2.1. Materials and chemicals

Platinum(II) acetylacetonate ($Pt(acac)_2$), Chloroplatinic acid hexahydrate, cetyltrimethylammonium bromide (CTAB), oleyl amine (OAm), Triton™ X-114, sodium tetrahydridoborate ($NaBH_4$) and perchloric acid (TraceSELECT) were all purchased from Sigma-Aldrich and used as received without further purification. Ultrapure water (18 MΩ cm) purified in a Millipore system was used in all experiments.

2.2. Preparation of regular PPNWs and PPNWs/C

The synthesis of regular Pt nanowires follows a previous method [24] with a slight modification. Specifically, 20 mg $Pt(acac)_2$, 50 mg CTAB, and 4 mL OAm were added into 20 mL high pressure vessel. After 30 min ultrasonication of these mixtures, the reaction vessel was dipped into an oil bath pre-heated at 170 °C. After 5 min, 20.3 mg $Mo(CO)_6$ was added into the reaction vessel to reduce $Pt(acac)_2$ at 170 °C for 2 h. The PPNWs product was precipitated by adding 10 mL ethanol, washed intensively with hexane, and finally dispersed in hexane. In current synthesis, once adding $Mo(CO)_6$ into a pre-heated OAm solution at 170 °C, $Mo(CO)_6$ decomposed to Mo atoms and CO molecules. Subsequently, Mo atoms would become MoO_x via reacting with oxygenated species such as trace H_2O and/or O_2 in the reaction system due to their strong oxyphilic attributes, while, CO molecules reduce Pt precursors to Pt atoms that grow into Pt nanowires with CTAB as a structurally-directing agent.

Ketjen black carbon was dispersed in 20 mL n-butylamine solvent, to which the regular PPNWs/hexane dispersion was poured, then dispersed thoroughly via ultrasonication, and stirred at room temperature for 24 h to allow for ligand exchange between oleyl amine and n-butylamine. The product was collected by centrifugation and washed with ethanol three times. To ensure complete removal of oleyl amine and/or n-butylamine adsorbed on PPNWs, the catalyst product was heated at 200 °C in air for 1 h in a muffle furnace. The Pt mass percentage was estimated to be 10.0 wt% by X-ray fluorescence (XRF).

2.3. Preparation of waved PPNWs and waved PPNWs/C

The synthesis of waved Pt nanowires follows a previous method [48]. Specifically, 0.25 mL Triton™ X-114 and 1 mL H_2PtCl_6 solution (15 mg_{Pt}/mL) were added into 50 mL H_2O and intensively stirred for 5 h. Then, 20 mL of freshly prepared $NaBH_4$ solution (1.5 mg/mL) was poured into the above solution to reduce H_2PtCl_6 and initiate the growth of waved PPNWs. The reaction was continued for 10 min without stirring. The product was collected by centrifugation, washed by ethanol/water solution (V/V=1/1) and finally dispersed in ethanol/water solution.

A waved PPNWs solution was poured into 50 mL ethanol/water solution (V/V=1/1) pre-dispersed with Ketjen black carbon. The resultant mixture was stirred for 24 h to allow for the deposition of waved PPNWs on Ketjen black The catalyst was collected by centrifugation and washed by ethanol/water solution. To remove residual Triton™ X-114 completely, the catalysts product was heated in air for 2 h. The Pt mass percentage was estimated to be 15.0 wt% by XRF.

2.4. Benchmark Pt/C catalyst

A commercial Pt/C (TEC10E20E) with an average particle size of 2 nm was obtained from Tanaka Kikinzoku Kogyo (TKK) and used as a reference catalyst.

3. Results and discussion

3.1. Catalyst characterization and ORR performance

We start from two model PPNWs: regular (Fig. 1a-d) and waved (Fig. 1e-h) PPNWs. Regular PPNWs were synthesized through reducing $Pt(acac)_2$ by $Mo(CO)_6$ and using cetyltrimethylammonium bromide as a soft template for the PPNWs growth in oleylamine solvent [24] while waved PPNWs via reducing H_2PtCl_6 by $NaBH_4$ and using Triton™ X-114 as a template in deionized water [48] (see the details in Supporting Information (SI)). The averaged-diameters of regular and waved PPNWs are 1.3 ± 0.3 and 2.2 ± 0.6 nm, respectively (Fig. S1). The most notable difference between two PPNWs is in the freedom of grains. Specifically, grains in regular PPNWs are restricted in 1D direction, while in waved PPNWs orientate quite freely in 3D directions, consequently appearing more disordered on wave PPNWs (see more in Figs. S2-S3).

We tested ORR performances of carbon-supported regular and waved PPNWs and a benchmark 2.0 nm Pt/C (TEC10E20E). Both regular and waved PPNWs/C display clearly anodically-shifted potentials for *OH/*O desorption and/or surface oxide reduction against 2 nm Pt/C, seen from their cathodic scans in cyclic voltammograms in Fig. 1(i). The ORR activities of regular and waved PPNWs/C surpass 2 nm Pt/C regarding Pt-based mass activity (MA, Fig. 1(k)) and electrochemical areas-based specific activity (SA, Fig. 1(l)). Notably, the SA activity on waved PPNWs/C is higher than on regular PPNWs/C, contrasted with the reports about an improved ORR activity on smaller-sized NWs. [19,21,22] Therefore, the waved PPNWs with a bit larger diameter display a higher activity against regular NWs, indicating a nanostructure-induced enhancement of ORR activity rather than a size effect. Specifically, nanoscale building blocks (i.e. 1–2 nm Pt grains) are similar for the three catalysts; the structural discrepancy accounting for their distinct ORR activities arises from grain organization patterns, i.e. isolated nanoparticles, regular PPNWs, and waved PPNWs. In other words, new structural factors and/or catalytically operating mechanisms are generated to enable enhanced ORR activity for PPNWs.

3.2. Atomistic analysis of structural defects in PPNWs

An intensive atomistic observation of randomly selected PPNWs demonstrates their polycrystalline nature without any observable single-crystalline NWs (Fig. 2, see more in Fig. S2). Structural heterogeneity appearing intra-NWs and inter-NWs calls for a sites-specific understanding of their properties. Overall, smaller-diameter PPNWs tend to present a larger defective/disordered degree. For instance, a large crystalline domain preferably emerges at 2.0 nm PPNWs (Fig. 2a), while an amorphous region arises for 1.2 nm PPNWs (Fig. 2b). A thorough examination of all measured PPNWs suggests two general defects: atomic steps and GBs. Notably, most of atomic steps in PPNWs are placed in planes (denoted as the plane-step different from the edge sites

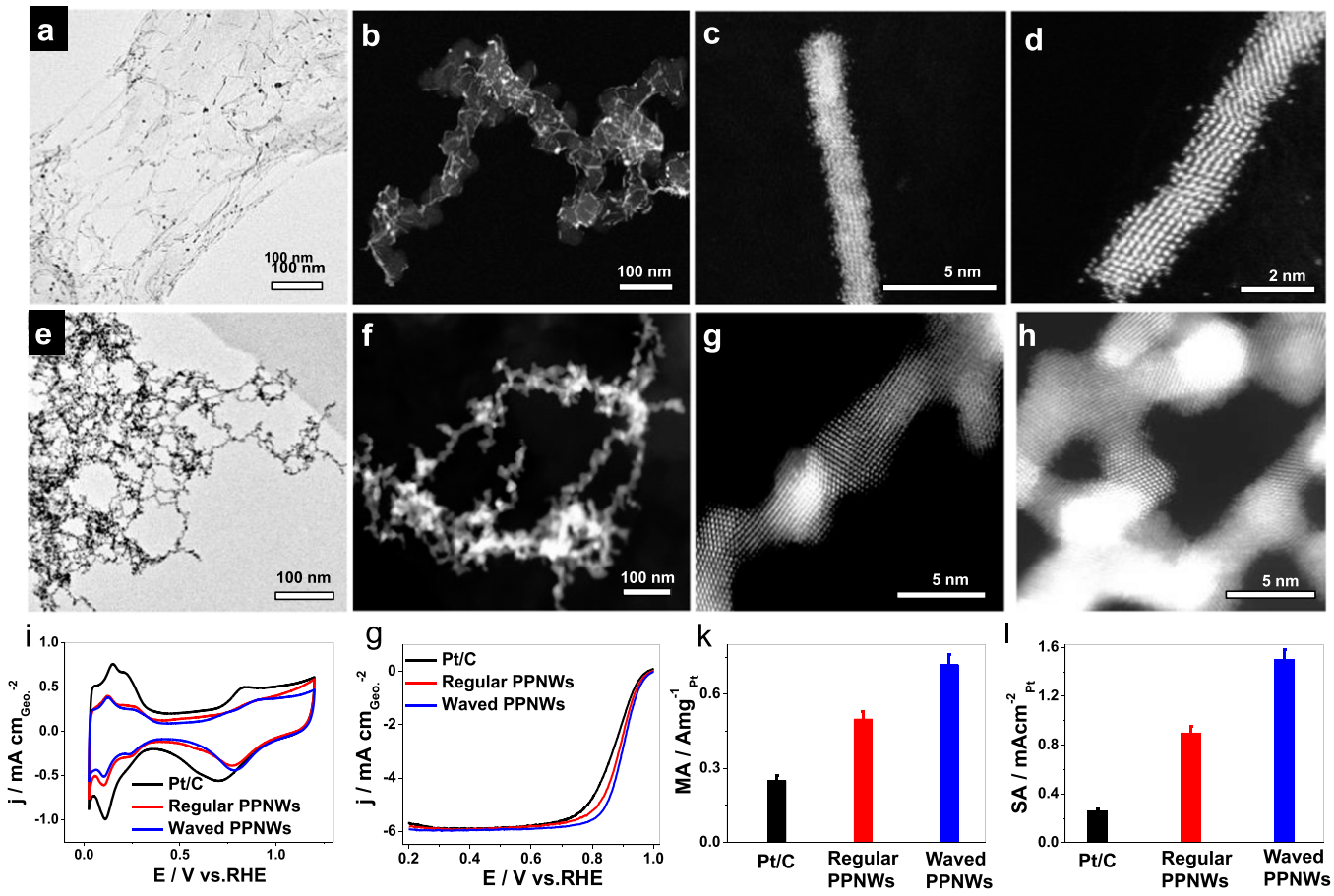

Fig. 1. : STEM images for (a-d) regular and (e-h) waved PPNWs, as-prepared (a, e) and carbon supported PPNWs (b-d, f-h). (i) Cyclic voltammograms measured in N_2-saturated 0.1 M $HClO_4$ aqueous electrolyte at 50 mV/s. (g) ORR anodic polarization curves measured at 20 mV/s (1600 rpm). (k-l) Histograms for mass activity (MA, k) and specific activity (SA, l) calculated by Koutecky-Levich equation to obtain mass transport-corrected kinetic current. Pt loadings on three electrodes are 12.0 μg_{Pt} $cm_{Geo.}^{-2}$.

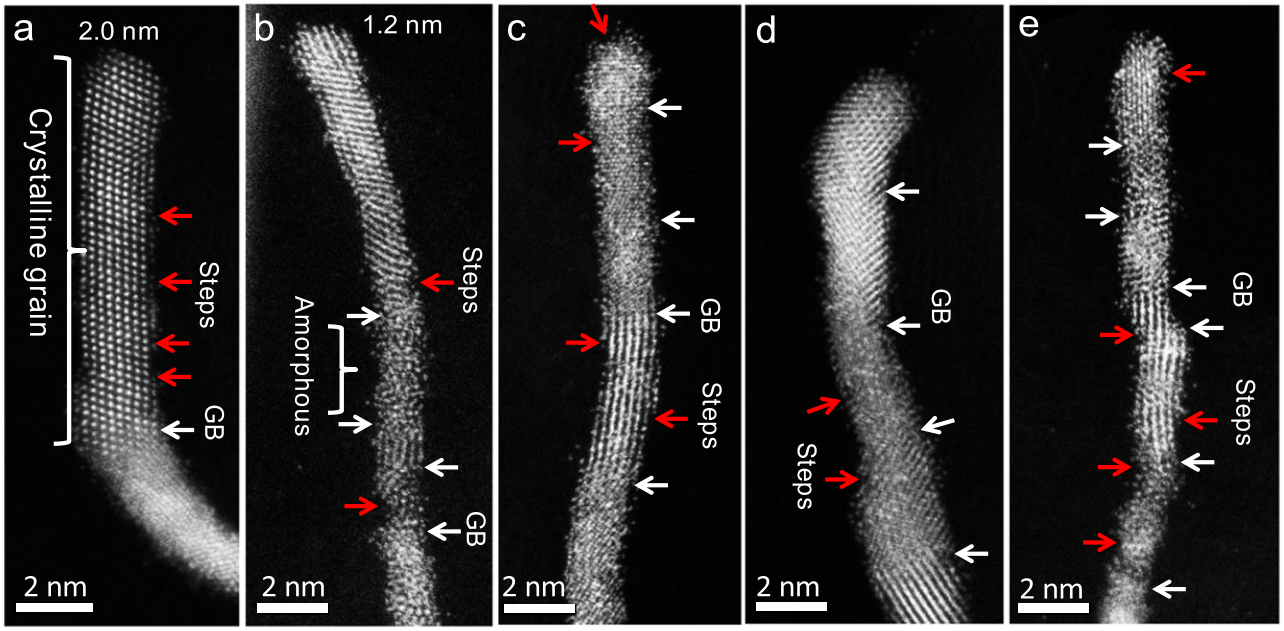

Fig. 2. : Atomistic observation of structural defects and heterogeneities of regular PPNWs. (a-e) HAADF-STEM images. Heterogeneous atomic structures are seen in intra- and inter-NWs, however two general defects, GBs (white arrows) and atomic steps (red arrows), are observable in all measured NWs.

of NPs in 2.0 nm Pt/C). We previously presented in situ spectroscopic evidence that those plane-steps on stepped nanofacets as templates disturb interfacial water network and thus destabilize ORR intermediates on vicinal terraces. [41] By contrast, edge sites over-binding with oxygen contribute negligibly to ORR activity for Pt NPs. [35,37,38] As plane-steps and edge sites have same coordination number (CN_{Pt-Pt}=7), their distinct contributions to ORR activity presumably originate from different geometry positions. We further through in-situ spectra discuss this point below.

We further measured atomistic images of waved PPNWs and found the similar results with regular PPNWs regarding plane-steps and GBs regardless of their varying nanostructures (Figs. 2–3). According to the sizes of misorientation angles (MOAs) and the excessive internal energy, GBs are classified into low-angle GBs (MOAs <15°) and high-angle GBs (MOAs >15°). [49] The twin is a special boundary between two grains with the relation of mirror reflection. Clearly, the grains in waved PPNWs orientate considerably freely and display large MOAs, resulting in a waved shape against regular PPNWs. Additionally, the stack fault and lattice deformation are observable around GBs (Figs. 3 and 4), as GBs could create dislocation pile-ups via hindering dislocation sliding. [49,50] Expectedly, high-angle GBs with larger MOAs via a dislocation-induced strain field cause more deformed/strained surface atoms [40] that are deviated from the ideal lattice positions and often display unusually catalytic activity. Given this, the overall larger MOAs inducing more catalytically active surface atoms may contribute to a higher ORR activity on waved PPNWs than on regular PPNWs. As the electrocatalyst structure might change dramatically in electrochemical environment and/or during electrolysis, we conducted TEM and HRTEM examination of steps and GBs in PPNWs after the ORR electrocatalysis. The TEM and HRTEM results shown in Figs. S6-S7 confirm the absence of dramatic structural change for both regular and waved PPNWs and the still-existing step and GB defects in PPNWs after the ORR electrolysis.

We measured atomic-resolution STEM images to directly present local lattice deformations and dislocations around GBs. At a glance, GBs in PPNWs bring about substantially structural heterogeneities regarding atomic dislocation and lattice distortion. The d spacings of local lattices around GBs (see domains A-E in Fig. 4a-d) vary on a case-by-case basis

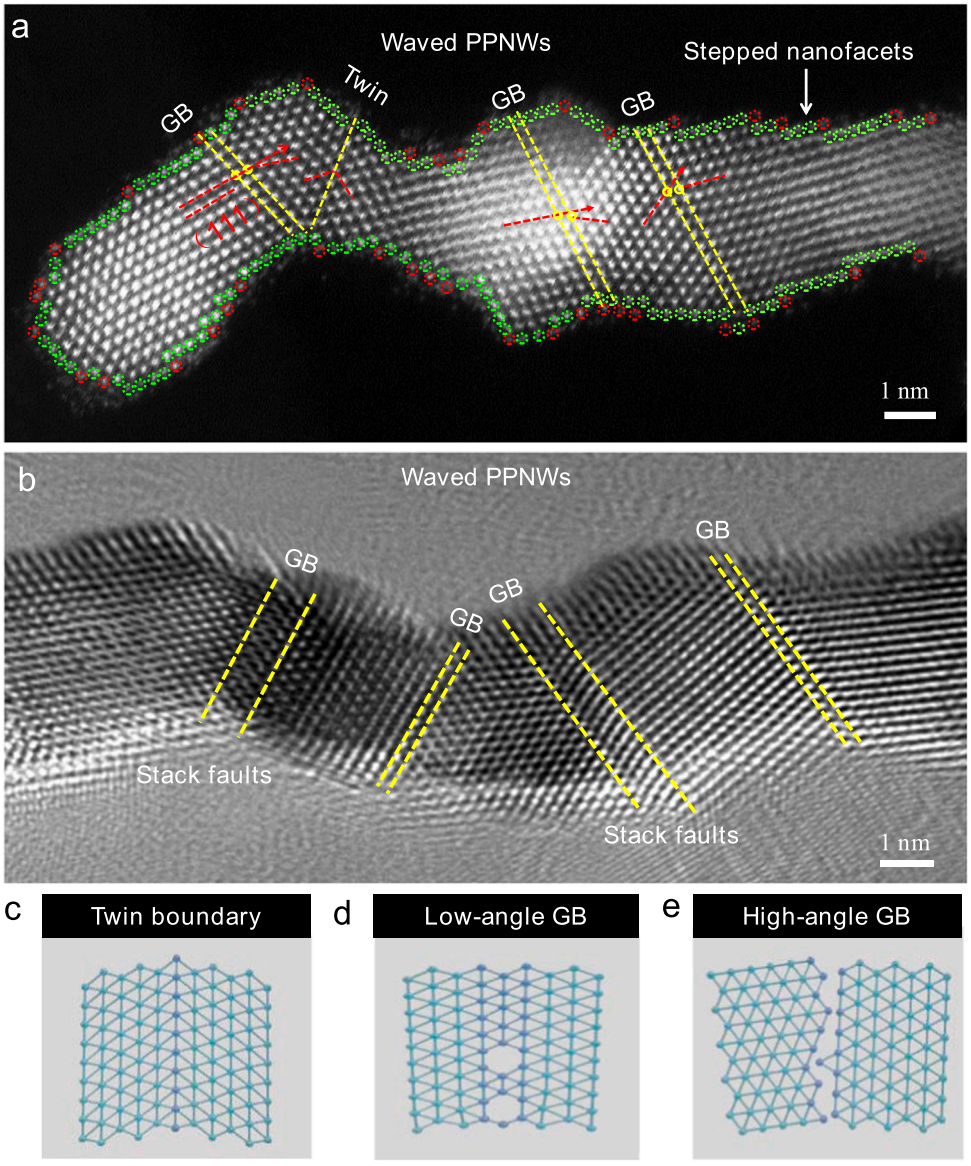

Fig. 3. : Atomistic observation of stepped nanofacets and GBs of waved PPNWs. (a) HAADF-STEM image and (b) high-resolution TEM image for waved PPNWs. Illustrations of structural models for (c) twin boundary, (d) low-angle GBs, and (e) high-angle GBs. [49] Red cycles in (a) suggest undercoordinated steps or kinks and green cycles represent terrace atoms.

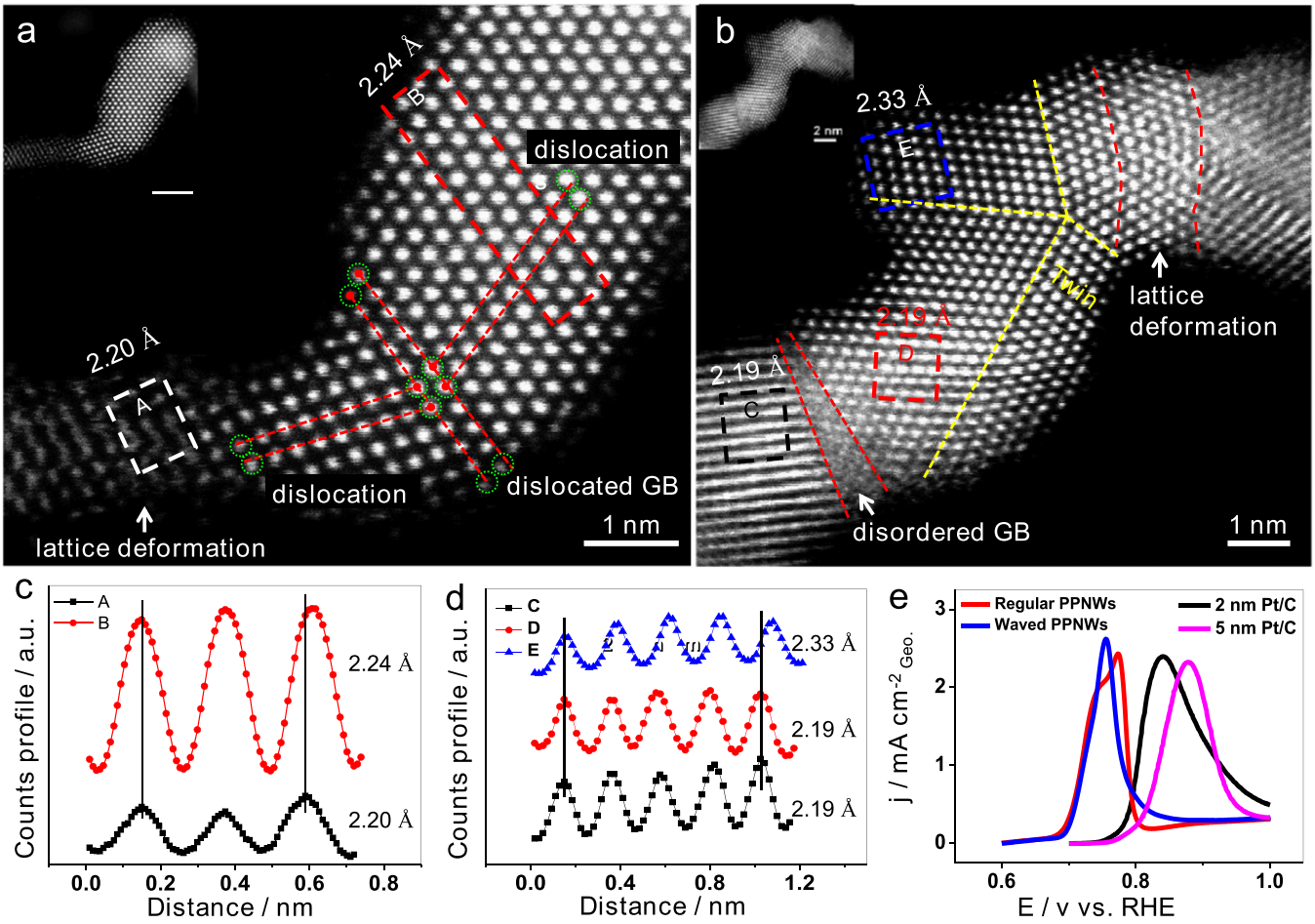

Fig. 4. Direct observation of local lattice deformation and dislocations. (a-b) Atomically-resolved STEM images. (c-d) Inter-planar spacings on selected local lattices. (e) Background-subtracted CO_{ads} stripping voltammograms; Pt loadings for 5 nm Pt/C is 17.8 μg_{Pt} cm^{-2}_{Geo} while for others are 12.0 μg_{Pt} cm^{-2}_{Geo}. The red dash lines in (a) indicate the dislocation defects, along which the atoms deviate from the "correct" positions in the crystal structure.

depending on local micro-environments such as the distances from GBs and edge, MOAs of GBs, and types of GBs (twin, low-angle and high-angle GBs). Of note, the domains A, C, and D appear quite contracted against the bulk Pt (111). Besides, the dislocation-induced microstrain is observable in domains nearby GBs (see the analysis marked by the "dislocation" in Fig. 4a). Meanwhile, GBs are a kind of structural defects to accommodate geometrically-misoriented neighboring grains (see Figs. 3–4), which could induce microstrain in and around GBs. Together, GBs not only themselves are disordered but also induce strain influence on neighboring grains. Expectedly, GBs and associated lattice microstrain tune d-state of surface Pt atoms and their affinity to reaction intermediates. [51,52] The STEM presents the definite visual images for the lattice deformation and strain, but they might be a species of the statistically-limited information, which is complemented by the ensemble-level electrochemical and XAFS data.

We first estimated samples-averaging defects from a structurally-sensitive *CO stripping reaction. [39,44,46] A 5.0 nm Pt/C (TEC10E50E-HT, 50.9 wt% obtained after a high-temperature heating treatment) was additionally examined for comparison. The kinetics of *CO electrooxidation is known accelerated by crystalline defects like undercoordinated sites via a bifunctional mechanism. [41,53,54] A cathodically-shifted *CO stripping peak on 2.0 nm Pt/C against 5 nm Pt/C (see Fig. 4e) demonstrates the defects active for *CO electrooxidation because 2.0 nm Pt/C has a significantly higher density of undercoordinated sites than 5.0 nm Pt/C. [35] However, both regular and wave PPNWs display enhanced *CO electrooxidation kinetics compared to 2 nm Pt/C, hard to rationalize from the view of the undercoordinated step or edge density. The PPNWs form through an oriented attachment of grains accompanied with disappearance of edges at grain connections. Thereby, a higher step or edge density would not appear in PPNWs than in a similar-size nanoparticulate counterpart. Assuming *CO electrooxidation kinetics were promoted by weakening *CO binding energy, the GBs-induced microstrain (e.g. the compressive lattice microstrain in some deformed domains, see Fig. 4a-b) may facilitate *CO electrooxidation, which was recently suggested by Chattot et al. [39,44] According to peak potentials of *CO electrooxidation, [39] the defects-induced microstrain follows a decreasing trend: waved PPNWs > regular PPNWs > 2 nm Pt/C.

3.3. *In-situ XAFS analysis of structural defects in PPNWs*

The ORR is a structurally-sensitive reaction. Meanwhile, Pt in ORR experiences the surface redox, associated site-blocking effect and interfacial interaction with adsorbates. These interrelated surface and interfacial processes in turn affect the proceeding of ORR on Pt, making a distinction of structural effects considerably challenging. [55] To this end, we traced Pt surface under ORR-relevant potentials using in situ XAFS (Fig. 5) by orderly applying constant potentials of 0.4, 0.7, and 0.9 V_{RHE}. The quasi-steady oxygenated species generated on Pt surface are captured by in-situ XAFS. Following by the ORR electrocatalysis, the in situ XAFS was measured (see experimental details in SI). For 2 nm Pt/C, the normalized white-line peak intensities of X-ray absorption near edge structure (XANES) at Pt-L_3 edge keep similar when increasing potentials from 0.4 to 0.7 V (vs. RHE) and then increases remarkably from

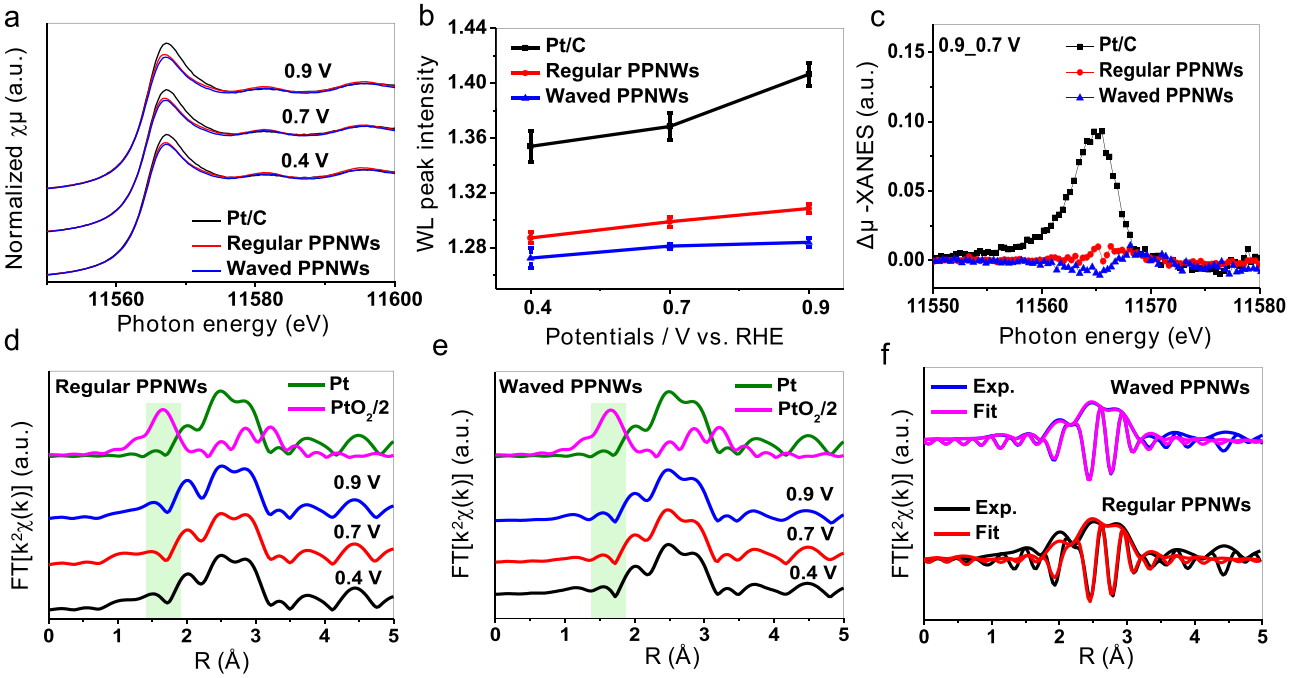

Fig. 5. : Operando XAFS to trace surface redox and structural parameters under ORR-relevant conditions. (a) XANES of working electrodes and (b) their white-line (WL) peak intensities. (c) Δμ-XANES spectra (0.9 V_0.7 V). (d-e) *In situ* EXAFS Fourier transforms of regular and waved PPNWs show only Pt-Pt scattering peaks when increasing potentials from 0.4 to 0.9 V_{RHE}. (f) Best fits of EXAFS for regular and waved PPNWs at 0.9 V_{RHE} in R space are obtained by only a Pt-Pt scattering shell.

0.7 to 0.9 V due to the *OH/*O bonding and/or surface oxide generation on Pt surface. By contrast, white-line peak intensities remain almost unchanged from 0.4 to 0.9 V for both regular and waved PPNWs (Fig. 5b). Both regular and waved PPNWs appear more metallic (i.e. smaller white line intensity) than 2 nm Pt/C (Fig. S4). We further used a $\Delta\mu_{Norm}$ method to reflect the amount and nature of adsorbates on electrodes (Fig. 5c). The difference peak areas of $\Delta\mu_{Norm}$ (0.9_0.7 V) = μ_{Norm}(0.9 V)-μ_{Norm}(0.7 V) decrease in the order: 2 nm Pt/C > > regular PPNWs ≈ waved PPNWs. Particularly, the difference peak intensities of $\Delta\mu_{Norm}$ (0.9_0.7 V) for regular and waved PPNWs are one order of magnitude smaller than that for 2 nm Pt/C. [41,56,57] The in situ XANES spectra certify that *OH/*O species electrochemically adsorbed on Pt at 0.9 V are hard to detect by XANES for regular and waved PPNWs, which is entirely different from the case of 2 nm Pt/C. This aspect indicates that those *OH/*O species are quite disordered and thereby their contribution to XANES is weak and even negligible, for which plane-steps can account via their template roles to deform interfacial water networks and bring about a change in interfacial solvation effect relative to Pt (111). [41,56–58] Consistent with XANES results, the best EXAFS fitting for 2 nm Pt/C needs a Pt−O scattering path due to the presence of discrete surface oxides (Fig. S5 and Table S1). By contrast, the in situ EXAFS and their curve-fits suggest only a Pt-Pt scattering shell for regular and waved PPNWs (Fig. 5d-f). Koper et al. recently demonstrated that adding Ni onto Pt(111) lowers barrier energies of interfacial water reorganization and thus facilitates proton transfer from water to electrodes [42]. Similarly, the proton transfer and oxygen gas transport from electrolyte to electrode in ORR require a significant rearrangement of interfacial water via hydrogen bonds [42, 59]. Given this, the disturbance of plane-steps to interfacial water via their template roles may accelerate proton transfer and consequently benefit proton-coupled electron transfer and ORR [17]. Notably, the edge sites of Pt NPs in 2 nm Pt/C did not result in remarkable disturbance of interfacial water networks, estimated from in situ XANES and EXAFS spectra in combination with electrochemical data (Fig. 1i). Additionally, edge sites are undercoordinated and their binding to oxygen is too strong to directly electrocatalyze the ORR. Thus, the direct and/or indirect contribution from edge sites is small or negligible for the ORR. STEM images showed there are a few of amorphous regions in PPNWs with the diameters less than 2 nm. The amorphous regions as a type of defects contain unsaturated sites and unordered domains. Similar with atomic steps, this disorder may also disturb interfacial water structure via hydrogen bonds, thereby regulating intermediate adsorption strengths and proton transfer in interfacial water networks.

As STEM images show different MOAs and associated microstrain between regular and waved PPNWs (Figs. 2–4), we further discuss this aspect from the bulk-averaging or ensemble EXAFS. The best fits of EXAFS at 0.4 V (a potential at electric double layer) show that the averaged Pt-Pt interatomic distances ($R_{Pt\text{-}Pt}$) are 2.755 ± 0.030, 2.755 ± 0.009 and 2.758 ± 0.007 Å for 2 nm Pt/C, regular PPNWs, and waved PPNWs, respectively (Table S1-S3). The difference in $R_{Pt\text{-}Pt}$ within fitting error is quite small for the three catalysts and seems hard to interpret their remarkably distinct ORR and *CO electrooxidation activity. Note that the EXAFS-derived $R_{Pt\text{-}Pt}$ is a bulk-averaging value probably masking the local heterogeneity, as shown in STEM images. We thus analyze their structural sources resulting in shortened $R_{Pt\text{-}Pt}$ against bulk Pt (2.775 Å). The $CN_{Pt\text{-}Pt}$ for 2 nm Pt/C is 8.3 ± 2.1, which is smaller than 10.7 ± 2.4 and 11.1 ± 1.0, respectively for the regular PPNWs and waved PPNWs (Table S1-S3). Undercoordinated surface atoms contract inward [41,60] either to stabilize the shared electron-pair bonds [61] or to smoothen the surface electronic density, [62,63] interpreting a shortened $R_{Pt\text{-}Pt}$ for 2 nm Pt/C with a high fraction of uncoordinated surface atoms, like edge and kink sites. However, a little larger $CN_{Pt\text{-}Pt}$ for the regular and waved PPNWs is expected to result in a bit longer $R_{Pt\text{-}Pt}$, which cannot account for their quite similar $R_{Pt\text{-}Pt}$ and thus suggest new structural sources to induce their shortened $R_{Pt\text{-}Pt}$ rather than the mentioned coordination-dependent surface contraction. [41,60] On this point, STEM images show direct evidence for the defects-induced microstrain (see Fig. 4). This is also supported by the studies of Chattot et al., [39,44] who suggested that the structure-sensitive *CO electrooxidation can reflect the trend in lattice microstrain or surface lattice distortion: waved PPNWs > regular PPNWs > 2 nm Pt/C (see Fig. 4e). The combined atomistic images, enhanced ORR and *CO electrooxidation activities, and in situ XANES and EXAFS spectra suggest that the plane-steps on stepped nanofacets and defect-induced microstrain

promote the ORR for the regular and waved PPNWs. Given this, the unusual size effect for PPNWs could be rationalized. As there are two variables, i.e. the degree of randomness/nanostructures and the diameter of nanowires affecting ORR activity, the comparison should be conducted under the condition of single variable. For two PPNWs with the same degree of randomness (e.g. both regular PPNWs), the PPNWs with smaller size show better ORR activity because the smaller the grains are, the larger the GBs concentration becomes, thus resulting in a larger fraction of strained surface atoms. In other words, the PPNWs with smaller diameters have more electroactive strained surface atoms that contribute to the enhancement of ORR activity. However, for two PPNWs with similar diameters or only a small difference in diameters, the degree of randomness may become a determining factor to ORR activity. For example, the waved PPNWs (2.2 ± 0.6 nm) with a bit larger diameter display a higher activity against regular NWs (1.3 ± 0.3 nm), which originates from that the larger degree of randomness and higher misorientation angles on waved PPNWs against regular PPNWs can induce larger structural micro-strain and more active strained Pt surface atoms for ORR. Additionally, Huang et al. recently revealed that the compressive strain in PPNWs leads to an increased the Pt vacancy formation energy, an indicator to describe the resistance to Pt dissolution [5]. Therefore, the structural micro-strain induced by GBs simultaneously benefits weakening oxygen adsorption energies and stabilizing nanowires, an implication for developing active and durable ORR electrocatalysts.

4. Conclusion

We explored molecular-level electroactive factors in model PPNWs and revealed electrocatalytic roles of GBs, plane-steps and a few of amorphous regions on the acidic ORR. As the local microstrain increase with the misorientation angles of GBs, the waved PPNWs with larger disorder showed a better ORR activity than the regular PPNWs. However, for two PPNWs with the same degree of randomness (e.g. both regular PPNWs), the PPNWs with smaller size would show better ORR activity. The plane-steps disturbs interfacial water networks via preferably hydrogen bonding, which destabilizes ORR intermediates on terraces and presumably promotes proton transfer; while the edge-sites hardly contribute ORR activity despite the same coordination number between them. Our experimental results and insights presented here should be valuable for a spectrum of heterogeneous electrocatalytic materials.

CRediT authorship contribution statement

Yasuhiro Iwasawa conceived the research and directed research. **Xiao Zhao** contributed to experiments and data analysis. Xiao Zhao and Shinobu Takao contributed to the HAADF-STEM analysis. **Xiao Zhao, Yusuke Yoshida, Takuma Kaneko, Takao Gunji, Kotaro Higashi, and Tomoya Uruga** contributed to the operando XAS analysis. The manuscript was primarily written by Xiao Zhao and Yasuhiro Iwasawa. All authors contributed to discussions and manuscript review.

Declaration of Competing Interest

The authors declare that they have no known competing financial interests or personal relationships that could have appeared to influence the work reported in this paper.

Data availability

Data will be made available on request.

Acknowledgement

This work was supported by New Energy and Industrial Technology Development Organization (NEDO), Ministry of Economy, Trade, and Industry (METI), Japan. XAFS measurements were performed with the approval of SPring-8 subject numbers 2017A7800, 2017A7801, 2017A7807, 2017A7808, 2017B7800, 2017B7801, 2017B7806, 2018A7800, 2018A7801, 2018A7806, 2018B7800, 2018B7801, 2019A7800, 2019A7801, 2019B7800, and 2019B7801. STEM measurements were partially conducted under the support of the NIMS microstructural characterization platform through the program "Nanotechnology Platform" of the Ministry of Education, Culture, Sports, Science and Technology (MEXT), Japan. Dr. X. Zhao thanks the support from the startup fund in Jilin University.

Appendix A. Supporting information

Supplementary data associated with this article can be found in the online version at doi:10.1016/j.apcatb.2022.122268.

References

[1] Y. Jiang, Y.-P. Deng, R. Liang, J. Fu, R. Gao, D. Luo, Z. Bai, Y. Hu, A. Yu, Z. Chen, d-Orbital steered active sites through ligand editing on heterometal imidazole frameworks for rechargeable zinc-air battery, Nat. Commun. 11 (2020) 5858.
[2] Y.-P. Deng, Y. Jiang, R. Liang, S.-J. Zhang, D. Luo, Y. Hu, X. Wang, J.-T. Li, A. Yu, Z. Chen, Dynamic electrocatalyst with current-driven oxyhydroxide shell for rechargeable zinc-air battery, Nat. Commun. 11 (2020) 1952.
[3] Y. Jiang, Y.-P. Deng, R. Liang, N. Chen, G. King, A. Yu, Z. Chen, Linker-compensated metal–organic framework with electron delocalized metal sites for bifunctional oxygen electrocatalysis, J. Am. Chem. Soc. 144 (2022) 4783–4791.
[4] L. Gao, T. Sun, X. Tan, M. Liu, F. Xue, B. Wang, J. Zhang, Y.-F. Lu, C. Ma, H. Tian, S. Yang, S.C. Smith, H. Huang, Trace doping of early transition metal enabled efficient and durable oxygen reduction catalysis on Pt-based ultrathin nanowires, Appl. Catal., B 303 (2022), 120918.
[5] Z. Yao, Y. Yuan, T. Cheng, L. Gao, T. Sun, Y. Lu, Y.-G. Zhou, P.L. Galindo, Z. Yang, L. Xu, H. Yang, H. Huang, Anomalous size effect of Pt ultrathin nanowires on oxygen reduction reaction, Nano Lett. 21 (2021) 9354–9360.
[6] L. Gao, X. Li, Z. Yao, H. Bai, Y. Lu, C. Ma, S. Lu, Z. Peng, J. Yang, A. Pan, H. Huang, Unconventional p–d hybridization interaction in PtGa ultrathin nanowires boosts oxygen reduction electrocatalysis, J. Am. Chem. Soc. 141 (2019) 18083–18090.
[7] P. Rao, D. Wu, T.-J. Wang, J. Li, P. Deng, Q. Chen, Y. Shen, Y. Chen, X. Tian, Single atomic cobalt electrocatalyst for efficient oxygen reduction reaction, eScience 2 (2022) 399–404.
[8] H. Yang, Y. Liu, X. Liu, X. Wang, H. Tian, G.I.N. Waterhouse, P.E. Kruger, S. G. Telfer, S. Ma, Large-scale synthesis of N-doped carbon capsules supporting atomically dispersed iron for efficient oxygen reduction reaction electrocatalysis, eScience 2 (2022) 227–234.
[9] X. Zhao, T. Gunji, F. Lv, B. Huang, R. Ding, J. Liu, M. Luo, Z. Zou, S. Guo, Direct observation of heterogeneous surface reactivity and reconstruction on terminations of grain boundaries of platinum, ACS Mater. Lett. 3 (2021) 622–629.
[10] X. Zhao, T. Gunji, T. Kaneko, S. Takao, T. Sakata, K. Higashi, Y. Yoshida, J. Ge, C. Liu, W. Xing, J. Zhu, M. Xiao, T. Uruga, F. Tao, Z. Chen, Evidence for interfacial geometric interactions at metal–support interfaces and their influence on the electroactivity and stability of Pt nanoparticles, J. Mater. Chem. A 8 (2020) 1368–1377.
[11] L. Zhao, C. Fu, L. Luo, J. You, L. An, X. Yan, S. Shen, J. Zhang, Electrochemical synthesis of monodispersed and highly alloyed PtCo nanoparticles with a remarkable durability towards oxygen reduction reaction, Appl. Catal., B 318 (2022), 121831.
[12] B.N. Ruggiero, K.M. Sanroman Gutierrez, J.D. George, N.M. Mangan, J. M. Notestein, L.C. Seitz, Probing the relationship between bulk and local environments to understand impacts on electrocatalytic oxygen reduction reaction, J. Catal. 414 (2022) 33–43.
[13] M. Luo, M.T.M. Koper, A kinetic descriptor for the electrolyte effect on the oxygen reduction kinetics on Pt(111), Nat. Catal. 5 (2022) 615–623.
[14] J. Huang, L. Sementa, Z. Liu, G. Barcaro, M. Feng, E. Liu, L. Jiao, M. Xu, D. Leshchev, S.-J. Lee, M. Li, C. Wan, E. Zhu, Y. Liu, B. Peng, X. Duan, W. A. Goddard, A. Fortunelli, Q. Jia, Y. Huang, Experimental Sabatier plot for predictive design of active and stable Pt-alloy oxygen reduction reaction catalysts, Nat. Catal. 5 (2022) 513–523.
[15] Q. Cheng, S. Yang, C. Fu, L. Zou, Z. Zou, Z. Jiang, J. Zhang, H. Yang, High-loaded sub-6 nm Pt1Co1 intermetallic compounds with highly efficient performance expression in PEMFCs, Energy Environ. Sci. 15 (2022) 278–286.
[16] C.-L. Yang, L.-N. Wang, P. Yin, J. Liu, M.-X. Chen, Q.-Q. Yan, Z.-S. Wang, S.-L. Xu, S.-Q. Chu, C. Cui, H. Ju, J. Zhu, Y. Lin, J. Shui, H.-W. Liang, Sulfur-anchoring synthesis of platinum intermetallic nanoparticle catalysts for fuel cells, Science 374 (2021) 459–464.
[17] T. Wang, Y. Zhang, B. Huang, B. Cai, R.R. Rao, L. Giordano, S.-G. Sun, Y. Shao-Horn, Enhancing oxygen reduction electrocatalysis by tuning interfacial hydrogen bonds, Nature, Catalysis 4 (2021) 753–762.

[18] R. Gao, J. Wang, Z.-F. Huang, R. Zhang, W. Wang, L. Pan, J. Zhang, W. Zhu, X. Zhang, C. Shi, J. Lim, J.-J. Zou, Pt/Fe2O3 with Pt–Fe pair sites as a catalyst for oxygen reduction with ultralow Pt loading, Nature, Energy 6 (2021) 614–623.
[19] K. Jiang, D. Zhao, S. Guo, X. Zhang, X. Zhu, J. Guo, G. Lu, X. Huang, Efficient oxygen reduction catalysis by subnanometer Pt alloy nanowires, Sci. Adv. 3 (2017) e1601705.
[20] S. Guo, S. Zhang, D. Su, S. Sun, Seed-mediated synthesis of Core/Shell FePtM/FePt (M = Pd, Au) nanowires and their electrocatalysis for oxygen reduction reaction, J. Am. Chem. Soc. 135 (2013) 13879–13884.
[21] C. Koenigsmann, A.C. Santulli, K. Gong, M.B. Vukmirovic, W.-p. Zhou, E. Sutter, S. S. Wong, R.R. Adzic, Enhanced electrocatalytic performance of processed, ultrathin, supported Pd-Pt core-shell nanowire catalysts for the oxygen reduction reaction, J. Am. Chem. Soc. 133 (2011) 9783–9795.
[22] C. Koenigsmann, W.-p Zhou, R.R. Adzic, E. Sutter, S.S. Wong, Size-dependent enhancement of electrocatalytic performance in relatively defect-free, processed ultrathin platinum nanowires, Nano Lett. 10 (2010) 2806–2811.
[23] S.H. Sun, F. Jaouen, J.P. Dodelet, Controlled growth of Pt nanowires on carbon nanospheres and their enhanced performance as electrocatalysts in PEM fuel cells, Adv. Mater. 20 (2008) 3900–3904.
[24] K. Li, X. Li, H. Huang, L. Luo, X. Li, X. Yan, C. Ma, R. Si, J. Yang, J. Zeng, One-nanometer-thick PtNiRh trimetallic nanowires with enhanced oxygen reduction electrocatalysis in acid media: integrating multiple advantages into one catalyst, J. Am. Chem. Soc. 140 (2018) 16159–16167.
[25] H. Liu, W. An, Y. Li, A.I. Frenkel, K. Sasaki, C. Koenigsmann, D. Su, R.M. Anderson, R.M. Crooks, R.R. Adzic, P. Liu, S.S. Wong, In situ probing of the active site geometry of ultrathin nanowires for the oxygen reduction reaction, J. Am. Chem. Soc. 137 (2015) 12597–12609.
[26] L. Bu, J. Ding, S. Guo, X. Zhang, D. Su, X. Zhu, J. Yao, J. Guo, G. Lu, X. Huang, A general method for multimetallic platinum alloy nanowires as highly active and stable oxygen reduction catalysts, Adv. Mater. 27 (2015) 7204–7212.
[27] H. Huang, K. Li, Z. Chen, L. Luo, Y. Gu, D. Zhang, C. Ma, R. Si, J. Yang, Z. Peng, J. Zeng, Achieving remarkable activity and durability towards oxygen reduction reaction based on ultrathin Rh-doped Pt nanowires, J. Am. Chem. Soc. 139 (2017) 8152–8159.
[28] Z.W. Chen, M. Waje, W.Z. Li, Y.S. Yan, Supportless Pt and PtPd nanotubes as electrocatalysts for oxygen-reduction reactions, Angew. Chem. Int. Ed. 46 (2007) 4060–4063.
[29] S.H. Sun, D.Q. Yang, D. Villers, G.X. Zhang, E. Sacher, J.P. Dodelet, Template- and surfactant-free room temperature synthesis of self-assembled 3D pt nanoflowers from single-crystal nanowires, Adv. Mater. 20 (2008) 571–574.
[30] N. Zhang, L. Bu, S. Guo, J. Guo, X. Huang, Screw thread-like platinum–copper nanowires bounded with high-index facets for efficient electrocatalysis, Nano Lett. 16 (2016) 5037–5043.
[31] B.Y. Xia, H.B. Wu, N. Li, Y. Yan, X.W. Lou, X. Wang, One-pot synthesis of Pt–Co alloy nanowire assemblies with tunable composition and enhanced electrocatalytic properties, Angew. Chem. Int. 54 (2015) 3797–3801.
[32] B.Y. Xia, H.B. Wu, Y. Yan, X.W. Lou, X. Wang, Ultrathin and ultralong single-crystal pt nanowire assemblies with highly stable electrocatalytic activity, J. Am. Chem. Soc. 135 (2013) 9480–9485.
[33] L. Bu, Y. Feng, J. Yao, S. Guo, J. Guo, X. Huang, Facet and dimensionality control of Pt nanostructures for efficient oxygen reduction and methanol oxidation electrocatalysts, Nano Res. 9 (2016) 2811–2821.
[34] M. Nesselberger, S. Ashton, J.C. Meier, I. Katsounaros, K.J.J. Mayrhofer, M. Arenz, The particle size effect on the oxygen reduction reaction activity of Pt catalysts: influence of electrolyte and relation to single crystal models, J. Am. Chem. Soc. 133 (2011) 17428–17433.
[35] M. Shao, A. Peles, K. Shoemaker, Electrocatalysis on platinum nanoparticles: particle size effect on oxygen reduction reaction activity, Nano Lett. 11 (2011) 3714–3719.
[36] M. Li, Z. Zhao, T. Cheng, A. Fortunelli, C.-Y. Chen, R. Yu, Q. Zhang, L. Gu, B. V. Merinov, Z. Lin, E. Zhu, T. Yu, Q. Jia, J. Guo, L. Zhang, W.A. Goddard III, Y. Huang, X. Duan, Ultrafine jagged platinum nanowires enable ultrahigh mass activity for the oxygen reduction reaction, Science 354 (2016) 1414–1419.
[37] A. Kulkarni, S. Siahrostami, A. Patel, J.K. Nørskov, Understanding catalytic activity trends in the oxygen reduction reaction, Chem. Rev. 118 (2018) 2302–2312.
[38] J.K. Nørskov, J. Rossmeisl, A. Logadottir, L. Lindqvist, J.R. Kitchin, T. Bligaard, H. Jónsson, Origin of the overpotential for oxygen reduction at a fuel-cell cathode, J. Phys. Chem. B 108 (2004) 17886–17892.
[39] R. Chattot, O. Le Bacq, V. Beermann, S. Kühl, J. Herranz, S. Henning, L. Kühn, T. Asset, L. Guétaz, G. Renou, J. Drnec, P. Bordet, A. Pasturel, A. Eychmüller, T. J. Schmidt, P. Strasser, L. Dubau, F. Maillard, Surface distortion as a unifying concept and descriptor in oxygen reduction reaction electrocatalysis, Nat. Mater. 17 (2018) 827–833.
[40] R.G. Mariano, K. McKelvey, H.S. White, M.W. Kanan, Selective increase in CO_2 electroreduction activity at grain-boundary surface terminations, Science 358 (2017) 1187–1192.
[41] X. Zhao, T. Gunji, T. Kaneko, Y. Yoshida, S. Takao, K. Higashi, T. Uruga, W. He, J. Liu, Z. Zou, An integrated single-electrode method reveals the template roles of atomic steps: disturb interfacial water networks and thus affect the reactivity of electrocatalysts, J. Am. Chem. Soc. 141 (2019) 8516–8526.
[42] I. Ledezma-Yanez, W.D.Z. Wallace, P. Sebastián-Pascual, V. Climent, J.M. Feliu, M. T.M. Koper, Interfacial water reorganization as a pH-dependent descriptor of the hydrogen evolution rate on platinum electrodes, Nat. Energy 2 (2017) 17031–17037.
[43] Z. Luo, H. Zhang, Y. Yang, X. Wang, Y. Li, Z. Jin, Z. Jiang, C. Liu, W. Xing, J. Ge, Reactant friendly hydrogen evolution interface based on di-anionic MoS2 surface, Nat. Commun. 11 (2020) 1116–1124.
[44] R. Chattot, T. Asset, P. Bordet, J. Drnec, L. Dubau, F. Maillard, Beyond strain and ligand effects: microstrain-induced enhancement of the oxygen reduction reaction kinetics on various PtNi/C nanostructures, ACS Catal. 7 (2017) 398–408.
[45] X. Zhao, S. Takao, K. Higashi, T. Kaneko, G. Samjeskè, O. Sekizawa, T. Sakata, Y. Yoshida, T. Uruga, Y. Iwasawa, Simultaneous improvements in performance and durability of an octahedral PtNix/C electrocatalyst for next-generation fuel cells by continuous, compressive, and concave Pt skin layers, ACS Catal. 7 (2017) 4642–4654.
[46] R. Chattot, I. Martens, M. Scohy, J. Herranz, J. Drnec, F. Maillard, L. Dubau, Disclosing Pt-bimetallic alloy nanoparticle surface lattice distortion with electrochemical probes, ACS Energy Lett. 5 (2020) 162–169.
[47] X. Zhao, S. Takao, T. Kaneko, Y. Iwasawa, Key factors for simultaneous improvements of performance and durability of core-shell Pt3Ni/carbon electrocatalysts toward superior polymer electrolyte fuel cell, Chem. Rec. 19 (2019) 1337–1353.
[48] X. Zhao, J. Zhang, L. Wang, H.X. Li, Z. Liu, W. Chen, Ultrathin PtPdCu nanowires fused porous architecture with 3D molecular accessibility: an active and durable platform for methanol oxidation, ACS Appl. Mat. Interfaces 7 (2015) 26333–26339.
[49] K. Lu, Stabilizing nanostructures in metals using grain and twin boundary architectures, Nat. Rev. Mater. 1 (2016) 16019–16031.
[50] H. Van Swygenhoven, Grain boundaries and dislocations, Science 296 (2002) 66–67.
[51] M. Mavrikakis, B. Hammer, J.K. Nørskov, Effect of strain on the reactivity of metal surfaces, Phys. Rev. Lett. 81 (1998) 2819–2822.
[52] M. Gsell, P. Jakob, D. Menzel, Effect of substrate strain on adsorption, Science 280 (1998) 717–720.
[53] D.S. Strmcnik, D.V. Tripkovic, D. van der Vliet, K.-C. Chang, V. Komanicky, H. You, G. Karapetrov, J.P. Greeley, V.R. Stamenkovic, N.M. Marković, Unique Activity of Platinum Adislands in the CO Electrooxidation Reaction, J. Am. Chem. Soc. 130 (2008) 15332–15339.
[54] N.P. Lebedeva, M.T.M. Koper, J.M. Feliu, R.A. van Santen, Role of crystalline defects in electrocatalysis: mechanism and kinetics of CO adlayer oxidation on stepped platinum electrodes, J. Phys. Chem. B 106 (2002) 12938–12947.
[55] A.M. Gomez-Marin, R.J. Rizo, J.M. Feliu, Oxygen reduction reaction at pt single crystals: a critical overview, Catal. Sci. Technol. 4 (2014) 1685–1698.
[56] X. Tian, X. Zhao, Y.-Q. Su, L. Wang, H. Wang, D. Dang, B. Chi, H. Liu, E.J. M. Hensen, X.W. Lou, B.Y. Xia, Engineering bunched Pt-Ni alloy nanocages for efficient oxygen reduction in practical fuel cells, Science 366 (2019) 850–856.
[57] Q. Jia, Z. Zhao, L. Cao, J. Li, S. Ghoshal, V. Davies, E. Stavitski, K. Attenkofer, Z. Liu, M. Li, X. Duan, S. Mukerjee, T. Mueller, Y. Huang, Roles of Mo surface dopants in enhancing the ORR performance of octahedral PtNi nanoparticles, Nano Lett. 18 (2018) 798–804.
[58] M.J. Kolb, R.G. Farber, J. Derouin, C. Badan, F. Calle-Vallejo, L.B.F. Juurlink, D. R. Killelea, M.T.M. Koper, Double-Stranded Water on Stepped Platinum Surfaces, Phys. Rev. Lett. 116 (2016) 136101–136105.
[59] T.J.F. Day, U.W. Schmitt, G.A. Voth, The mechanism of hydrated proton transport in water, J. Am. Chem. Soc. 122 (2000) 12027–12028.
[60] W.J. Huang, R. Sun, J. Tao, L.D. Menard, R.G. Nuzzo, J.M. Zuo, Coordination-dependent surface atomic contraction in nanocrystals revealed by coherent diffraction, Nature, Mater 7 (2008) 308–313.
[61] L. Pauling, Atomic radii and interatomic distances in metals, J. Am. Chem. Soc. 69 (1947) 542–553.
[62] M.W. Finnis, V. Heine, Theory of lattice contraction at aluminium surfaces, J. Phys. F: Met. Phys. 4 (1974) L37–L41.
[63] R. Smoluchowski, Anisotropy of the electronic work function of metals, Phys. Rev. 60 (1941) 661–674.